Algorithm for time-delay interferometry numerical simulation and sensitivity investigation

Gang Wang,[1,*] Wei-Tou Ni,[2,3,4,†] Wen-Biao Han,[1,5,6,7,8,‡] and Cong-Feng Qiao[9,10,§]

[1]*Shanghai Astronomical Observatory, Chinese Academy of Sciences, Shanghai 200030, China*
[2]*National Astronomical Observatories, Chinese Academy of Sciences, Beijing 100012, China*
[3]*State Key Laboratory of Magnetic Resonance and Atomic and Molecular Physics, Innovation Academy for Precision Measurement Science and Technology (APM), Chinese Academy of Sciences, Wuhan 430071, China*
[4]*Department of Physics, National Tsing Hua University, Hsinchu, Taiwan 30013, Republic of China*
[5]*School of Astronomy and Space Science, University of Chinese Academy of Sciences, Beijing 100049, China*
[6]*School of Fundamental Physics and Mathematical Sciences, Hangzhou Institute for Advanced Study, UCAS, Hangzhou 310024, China*
[7]*International Centre for Theoretical Physics Asia-Pacific, Beijing/Hangzhou, China*
[8]*Key Laboratory for Research in Galaxies and Cosmology, Shanghai Astronomical Observatory, Shanghai 200030, China*
[9]*School of Physics, University of Chinese Academy of Sciences, Beijing 100049, China*
[10]*CAS Center for Excellence in Particle Physics, Beijing 100049, China*

(Received 29 October 2020; accepted 2 June 2021; published 24 June 2021)

We introduce a generic algorithm to determine the time delays and spacecraft positions to compose any time-delay interferometry (TDI) channel in the dynamical case and evaluate its sensitivity by using a full numerical method. We select 11 second-generation TDI channels constructed from four approaches and investigate their gravitational wave responses, noise levels, and averaged sensitivities under a numerical LISA orbit. The sensitivities of selected channels are various especially for frequencies lower than 20 mHz. The optimal channel A_2 (or equivalently E_2) combined from second-generation Michelson TDI channels (X_1, X_2, and X_3) achieves the best sensitivity among the channels, while the Sagnac α_1 channel shows the worst sensitivity. Multiple channels show better sensitivities at some characteristic frequencies compared to the fiducial X_1 channel. The joint $A_2 + E_2 + T_2$ observation not only enhances the sensitivity of the X_1 channel by a factor of $\sqrt{2}$ to 2, but also improves the capacity of sky coverage.

DOI: 10.1103/PhysRevD.103.122006

I. INTRODUCTION

Advanced LIGO and Advanced Virgo have observed a score of gravitational wave (GW) signals since the first detection of binary black hole (BH) coalescence—GW150914 ([1–9], and references therein). Most of the detections were identified as binary BH systems, and two events were recognized as binary neutron star coalescence [3,6]. The recently announced detection, GW190521, was inferred as an intermediate mass BH coalescence [10].

LISA is scheduled to be launched around the 2030s and will target detection of the GW in the frequency range 0.1 mHz to 100 mHz. By employing drag-free technology, three spacecraft (S/C) will follow their respective geodesics to form a triangular laser interferometer with an arm length of 2.5×10^6 km. If traditional laser metrology is utilized for the long and unequal interferometric arms, the laser frequency noise will be too overwhelming to detect the GW signals. To achieve the targeted sensitivity, time-delay interferometry (TDI) is proposed for the LISA to suppress the laser frequency noise. In the previous literature, TDI has been well studied and demonstrated for the first generation ([11–19], and references therein), and the second generation ([20–27], and the references therein). The first-generation TDI configurations are designed to cancel the laser noise for a static constellation. The second-generation TDI is proposed to suppress laser frequency fluctuations in the case of time-varying arm lengths up to the first order derivative, and solves a more realistic situation.

With the implementation of TDI, the secondary noises and GW signals could be accumulated or canceled with the paths combination. The acceleration noise and the optical

*gwang@shao.ac.cn, gwanggw@gmail.com
†weitou@gmail.com
‡wbhan@shao.ac.cn
§qiaocf@ucas.ac.cn

path noise are supposed to be the leading noises in the second-generation TDI. The cancellations and suppressions of other secondary noises are in an active study stage. For instance, the clock jitter noise could be reduced using new measurement combinations [24,28–30], and the tilt-to-length noise could be resolved by a new optical design [31,32]. The GW response in the TDI channels could also be suppressed or enhanced by the path combination. To investigate the noise level and GW response in TDI channels, multiple simulators have been developed for the LISA mission with different focuses [17,18,25,33,34]. Considering the complexity of the TDI calculation, most of the investigations implemented the analytical or semi-analytical algorithms for the calculations.

We have developed a numerical algorithm to calculate the path mismatches in TDI for LISA-like missions and ASTROD-GW concept since 2011 [35–43]. In previous work [44], by using a set of numerical orbit, we investigated the GW responses, noise levels and sensitivities of the first-generation TDI channels for LISA and TAIJI. We adopted a semi-analytical approach to evaluate the GW response and secondary noises in an instantaneous static TDI configuration, and implemented the numerical method to calculate the laser frequency noise raised by the path mismatches in a dynamic TDI configuration. For the second-generation TDI, their configurations could be flexibly constructed from different approaches ([20,22,23,26,45], and references therein). Therefore, due to the versatility and flexibility of path combinations, the complexity of analytical evaluation would significantly increase to adapt to various TDI channels. Furthermore, compared to the first-generation TDI, the second-generation TDI would involve more links in a wider time span and the static approximation would increase the inaccuracy of the calculations.

To investigate TDI performances in the realistic dynamical case, by using numerical mission orbit data and an ephemeris framework, we start from our previous algorithm which can determine the S/C positions and laser propagation time between S/C incorporating relativistic time delays during TDI. We also develop new modules in this work to thoroughly evaluate the GW response, noise level, and sensitivity for any TDI observable by using a numerical algorithm. As a preparation for algorithm implementation, a S/C layout-time delay diagram is employed to illustrate the paths of a TDI channel and streamline the calculation procedures. We select 11 second-generation TDI channels constructed from four approaches, and investigate their yearly averaged sensitivities. The investigations show that mismatches of laser paths in selected channels are sufficiently decreased and could make the laser frequency noise well below the secondary noises. The optimal channels A_2/E_2 combined from second-generation Michelson TDI channels (X_1, X_2, and X_3) achieves the best sensitivity in selected channels for frequencies lower than 50 mHz, while the Sagnac α_1 channel shows the worst sensitivity. Multiple TDI channels could have better sensitivities at some characteristic frequencies compared to the fiducial X_1 channels. The sensitivities of Michelson-type TDI channels would be identical considering the noise level increase or decrease with the GW response increase or decrease.

This paper is organized as follows: In Sec. II, we introduce the numerical algorithm to determine the time delay and S/C positions in TDI, and the selected TDI channels constructed from different approaches. In Sec. III, we present the TDI response calculation by using the obtained time delay and S/C positions, and analyze the yearly averaged responses for the selected channels. In Sec. IV, we examine laser frequency noise due to the path mismatch in TDI channels, and numerically evaluate the noise levels generated from the acceleration noise and the optical path noise. In Sec. V, we synthesize yearly averaged sensitivities of each TDI channel, and compare their sensitivities with the fiducial first-generation Michelson X channel. We give our conclusions in Sec. VI. (We set $G = c = 1$ in this work except where specified in the equations.)

II. TIME DELAY DETERMINATION AND TDI CHANNEL SELECTIONS

A. Algorithm for TDI diagram

The purpose of TDI is to construct the equivalent equal arm interferometer by combining multiple arm links in sequence and to cancel laser frequency noise. The path matching of a TDI configuration depends on the arm lengths and relative motions between the S/C. A numerical LISA orbit is utilized in this investigation as shown in Fig. 2 of [46]. The orbit is achieved based on the LISA 2017 requirements that the amplitudes of relative velocities between S/C are less than 5 m/s for 2.5×10^6 km arm length [47]. The original LISA optical design is to equip two optical benches on each S/C and collect two measurements on each optical bench ([12,17,18], and references therein). A newly designed configuration has been proposed that three or four measurements are gathered on each optical bench to remove some secondary noise more effectively ([24,25,28,29], and references therein). We employ the newly designed measurements on each optical bench in this work.

The expressions of the first-generation TDI channels have been formulated in previous works [11–14,16–20,22,23], and the expression of measurements in the Michelson-X channel could be simplified as

$$\begin{aligned} \mathrm{X} = &[\eta_{31} + \mathcal{D}_{31}\eta_{13} + \mathcal{D}_{13}\mathcal{D}_{31}\eta_{21} + \mathcal{D}_{21}\mathcal{D}_{13}\mathcal{D}_{31}\eta_{12}] \\ &- [\eta_{21} + \mathcal{D}_{21}\eta_{12} + \mathcal{D}_{12}\mathcal{D}_{21}\eta_{31} + \mathcal{D}_{31}\mathcal{D}_{12}\mathcal{D}_{21}\eta_{13}], \end{aligned} \quad (1)$$

by implementing the combined observables η_{ji} for S/Cj to S/Ci ($j \to i$) as defined in [24,28,29],

$$\eta_{ji} = s_{ji} + \frac{1}{2}[\tau_{ij} - \varepsilon_{ij} + \mathcal{D}_{ji}(2\tau_{ji} - \varepsilon_{ji} - \tau_{jk})]$$
$$\text{for } (2 \to 1), (3 \to 2) \text{ and } (1 \to 3),$$
$$\eta_{ji} = s_{ji} + \frac{1}{2}[\tau_{ij} - \varepsilon_{ij} + \mathcal{D}_{ji}(\tau_{ji} - \varepsilon_{ji}) + \tau_{ik} - \tau_{ij}]$$
$$\text{for } (1 \to 2), (2 \to 3) \text{ and } (3 \to 1), \quad (2)$$

where s_{ji}, ε_{ij} and τ_{ij} are described in Appendix, $\mathcal{D}_{ij}$ is a time-delay operator and acts on a measurement $y(t)$ by

$$\mathcal{D}_{ij}y(t) = y(t - L_{ij}(t)),$$
$$\mathcal{D}_{mn}\mathcal{D}_{ij}y(t) = y(t - L_{ij}(t) - L_{mn}(t - L_{ij}(t))),$$
$$\cdots \quad (3)$$

To visualize the paths of TDI and streamline the calculations, we developed a S/C layout-time delay diagram for TDI configurations [36] (Muratore *et al.* [26] developed their similar space-time diagram in recent work). The diagrams for four first-generation TDI channels are shown in Fig. 1. The x-axis shows the spatial separation between the S/C, and the y-axis shows the time direction. Each vertical line indicates the trajectory of one S/C with time (ⓘ indicates S/Ci, $i = 1, 2, 3$), and the ticks on the y-axis show the value of the time delay with respect to the TDI ending time $\tau = 0$. We clarify that $t_{\rm rel}$ is the time with respect to the starting time t_0 at starting S/C of TDI. To avoid paths crossing at noninteger delay times and display the paths clearly, the extra trajectory lines are plotted for S/C2 (dotted green lines) and S/C3 (dashed orange lines). The blue lines show the paths of the TDI channels, the solid line and the dashed line indicate two groups of interfered laser beams, as well as the signs in the TDI expression.

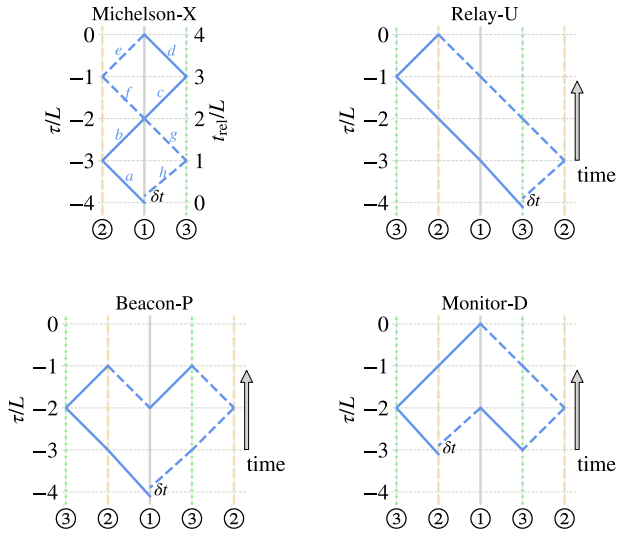

FIG. 1. The S/C layout-time delay diagrams for the first-generation TDI channels Michelson-X, Relay-U, Beacon-P, and Monitor-D. The vertical lines indicate the trajectories of S/C in the time direction (ⓘ indicates S/Ci, $i = 1, 2, 3$), and the ticks on each y-axis show the value of time delay with respect to the TDI ending time $\tau = 0$. The $t_{\rm rel}$ is the time with respect to the starting time t_0 at starting S/C of TDI. To avoid the crossing caused by TDI paths at noninteger delay times and show the paths clearly, extra trajectory lines are plotted for S/C2 (dotted green lines) and S/C3 (dashed orange lines). The blue lines show the paths of TDI channels, the solid line and dashed line indicate two groups of interfered laser beams.

We select the Michelson-X to specify the procedures of diagram implementation as shown in the upper left plot of Fig. 1 and Table I. The calculation starts from the mission time $t_0 = 0$ at point $\xi(①; t_{\rm rel} = 0; \tau \simeq -4L)$ toward the $\xi(②; t_{\rm rel} = L_{12}; \tau \simeq -3L)$ [the link a, corresponding to the last term in the first row of Eq. (1)], and determines the relative time $t_{\rm rel} = 8.3474947$ s with respect to t_0 and registers the position of ② at the time $t_0 + t_{\rm rel}$. Along the link b, the second step starts from $\xi(②; t_{\rm rel} = 8.3474947\text{s}; \tau \simeq -3L)$ to $\xi(①; t_{\rm rel} = L_{12} + L_{21}; \tau \simeq -2L)$, and updates the relative time $t_{\rm rel} = 16.6934247$ s and registers the position of ① at updated $t_0 + t_{\rm rel}$. The steps are implemented based on alphabetical order from the link c until final link h by using the same method. For the links with backward time direction, a minus sign will be implemented which corresponds to the terms with minus signs in Eq. (1). The process of each step could be expressed as

$$l\text{th link}: \xi(\boldsymbol{r}_{i,l-1}; t_{{\rm rel},l-1}; \tau_{i,l-1}) \mapsto \xi(\boldsymbol{r}_{j,l}; t_{{\rm rel},l}; \tau_{j,l}). \quad (4)$$

After all steps are implemented, the final ending S/C will be the initial sending S/C. The relative time $t_{\rm rel}$ would differ from the starting $t_{\rm rel} = 0$ due to the relative motion between the S/C during TDI which is the path mismatch δt. In previous work [36–43], we implemented this algorithm to calculate the path mismatch for laser frequency noise suppression and verify the feasibility of

TABLE I. The results of the first-generation Michelson-X channel calculation in each step at staring mission time $t_0 = 0$. The delay time is determined from the relative time $t_{\rm rel}$ by $\tau = t_{\rm rel} - \max(t_{\rm rel})$. (Only the first seven decimals are present for time factors).

Step l	Mission time t_0	Relative time $t_{\rm rel}$ (s)	Delay time τ (s)	S/C	Position (SSB)[a]
0	0	0	−33.4510480	1	$\boldsymbol{r}_1$
1	0	8.3474947	−25.1035533	2	$\boldsymbol{r}_2$
2	0	16.6934247	−16.7576233	1	$\boldsymbol{r}_1$
3	0	25.0728702	−8.3781778	3	$\boldsymbol{r}_3$
4	0	33.4510480	0	1	$\boldsymbol{r}_1$
5	0	25.1051181	−8.3459299	2	$\boldsymbol{r}_2$
6	0	16.7576236	−16.6934244	1	$\boldsymbol{r}_1$
7	0	8.3794460	−25.0716020	3	$\boldsymbol{r}_3$
8	0	6.3697e-7	−33.4510474	1	$\boldsymbol{r}_1$

[a]the positions in the solar-system barycentric coordinates.

TDI configurations. Another purpose of the calculation is to determine time delay in each link and the S/C positions, since the response to a GW signal will depend on the time delay factors and instantaneous positions of S/C, and the noises in TDI channels are related to the time delay.

For a TDI channel, the time at the top vertex point is defined as $t_m = t_0 + \max(t_{\rm rel})$ and time delay is set to be $\tau = 0$ except for the Beacon-P configuration, and then the time delay at each step is calculated by $t_{\rm rel} - \max(t_{\rm rel})$. The results of each step for the Michelson-X channel at starting mission time are shown in Table I.

The combined measurement of one TDI channel is the sum of each step,

$$\mathrm{TDI} = \sum_{l=1}^{n} \mathrm{sgn}(\tau_l - \tau_{l-1}) \eta_{ij,l}(t_m + \tau_{j,l}), \tag{5}$$

with sign function

$$\mathrm{sgn}(\tau_l - \tau_{l-1}) = \begin{cases} 1 & \text{if } \tau_l - \tau_{l-1} > 0 \\ -1 & \text{if } \tau_l - \tau_{l-1} < 0. \end{cases} \tag{6}$$

B. Time delay calculation

The time delay between the laser beam sender and receiver is essential for TDI calculations as aforementioned. Due to the gravitational field of celestial bodies, there will be extra relativistic time delay during the light propagation besides the delay from coordinate distance, and its leading order is required to be considered during the calculation [48]. The time delay from the sending time T^s at $\boldsymbol{r}_1$ to the receiving time T^r at $\boldsymbol{r}_2$ is calculated by [49,50]

$$T^r - T^s = \frac{R}{c} + \Delta T_{\rm PN}, \tag{7}$$

where R is the coordinate distance between the sender and receiver S/C, c is speed of light, and $\Delta T_{\rm PN}$ is the relativistic time delay caused by the gravitational field

$$\Delta T_{\rm PN} = \frac{2GM}{c^3} \ln\left(\frac{R_1 + R_2 + R}{R_1 + R_2 - R}\right) + \frac{G^2M^2}{c^5} \frac{R}{R_1 R_2} \left[\frac{15}{4} \frac{\arccos(\mathbf{N}_1 \cdot \mathbf{N}_2)}{|\mathbf{N}_1 \times \mathbf{N}_2|} - \frac{4}{1 + \mathbf{N}_1 \cdot \mathbf{N}_2}\right], \tag{8}$$

where G is gravitational constant, M is the gravitational body, $\mathbf{N}_1$ and $\mathbf{N}_2$ are the respective unit vector from the gravitating body to the sender and receiver, and R_1 and R_2 are the radial distances of the sender and the receiver from a gravitating body. The leading order relativistic time delay caused by gravitational field of the Sun is included in our current calculation; the effects from other planets should be lower orders than the Sun for the LISA mission.

On the other hand, due to the relative motion between S/C, the displacement of the receiver during the light propagation is also considered. The receiving time is determined by using iteration in numerical calculation,

$$\begin{aligned} T_0^r &= T_0^s + T_1 + T_2 + T_3 + \cdots \\ T_1 &= \frac{|\boldsymbol{r}_r(T_0^s) - \boldsymbol{r}_s(T_0^s)|}{c} + \Delta T_{1,\rm PN} \\ T_1 + T_2 &= \frac{|\boldsymbol{r}_r(T_0^s + T_1) - \boldsymbol{r}_s(T_0^s)|}{c} + \Delta T_{2,\rm PN} \\ T_1 + T_2 + T_3 &= \frac{|\boldsymbol{r}_r(T_0^s + T_1 + T_2) - \boldsymbol{r}_s(T_0^s)|}{c} + \Delta T_{3,\rm PN} \\ &\cdots \end{aligned} \tag{9}$$

During the iteration calculation, the Chebyshev polynomial interpolation is utilized to precisely obtain the position of a S/C at any moment [51,52].

C. Selection of TDI channels

For the first-generation TDI, there are five recognized configurations which are Sagnac, Michelson, Relay, Beacon, and Monitor. However, the configurations of the second-generation TDI are more flexible and could be constructed from different approaches ([20,22,23,26,45], and references therein). In this work, we select 11 typical TDI channels derived from four methods as follows:

(a) The first group of the second-generation TDI channels is derived from the same two first-generation TDI channels, and the channels are constructed from two same first-generation channels with a relative time shift. The expressions could be described as

$$\begin{aligned} \mathrm{X}_1(t) &\approx \mathrm{X}(t - 4L) - \mathrm{X}(t), \\ \alpha_1(t) &\approx \alpha(t - 3L) - \alpha(t), \\ \mathrm{U}_1(t) &\approx \mathrm{U}(t - 2L) - \mathrm{U}(t), \\ \mathrm{P}_1(t) &\approx \mathrm{P}(t - L) - \mathrm{P}(t + L), \\ \mathrm{D}_1(t) &\approx \mathrm{D}(t - 2L) - \mathrm{D}(t). \end{aligned} \tag{10}$$

The subscript 1 indicates the first channel of second-generation TDI combining with its first-generation family. Using four first-generation TDI channels from each configuration shown in Fig. 1, the corresponding second-generation diagrams are shown in Fig. 2. The approximation is used to emphasize that the time delay between two TDI channels is not exactly equal to the integer times of arm length in numerical calculation. Similar to the first-generation, as we can expect, the performances of P/P_1 and D/D_1 will be identical. And we will choose P/P_1 to represent these two configurations in the following investigations.

(b) The second group of TDI channels is the optimal channels combined from three channels of one

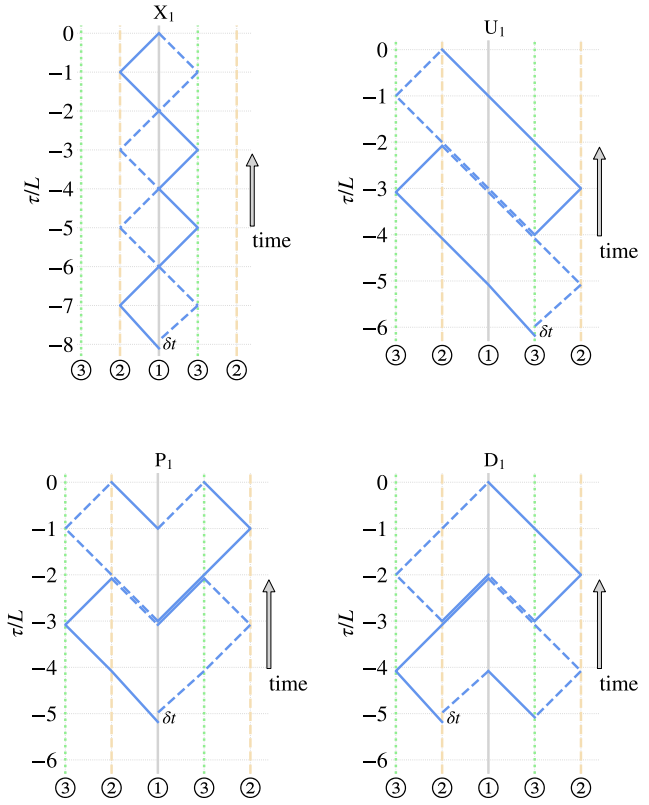

FIG. 2. The diagrams of the second-generation TDI channels Michelson-X_1, Relay-U_1, Beacon-P_1 and Monitor-D_1 constructed respectively from two same first-generation channels with a relative time shift.

configuration. Similar to the optimal TDI channels, (A, E, and T), generated from three first-generation Michelson channels (X, Y, and Z) [53,54], three optimal channels can be constructed from the second-generation Michelson channels (X_1, X_2, and X_3, the X_2 and X_3 channels are obtained by cyclical permutation of the spacecraft indices from X_1) by using the corresponding linear combinations

$$\begin{aligned} A_2 &= \frac{X_3 - X_1}{\sqrt{2}}, \\ E_2 &= \frac{X_1 - 2X_2 + X_3}{\sqrt{6}}, \\ T_2 &= \frac{X_1 + X_2 + X_3}{\sqrt{3}}. \end{aligned} \tag{11}$$

A_2 and E_2 are also expected to have equivalent performance, and we choose the A_2 channel to represent the results.

(c) The third group is the extended TDI channels from two different first-generation channels. A second-generation TDI channel could be formed by combining one first-generation TDI channel with its time flipped one. The Monitor-D channel could be recognized as a time flipped Beacon-P as shown in Fig. 1, and their combination is named PD as shown in Fig. 3. Moreover, the diagram could also indicate the reason for the identical performance of Beacon and Monitor as we have shown in [44]. The $\bar{U}$ denotes the flipped U channel, and the combined channel is named $U\bar{U}$ as shown in Fig. 3. Their expressions could be described as

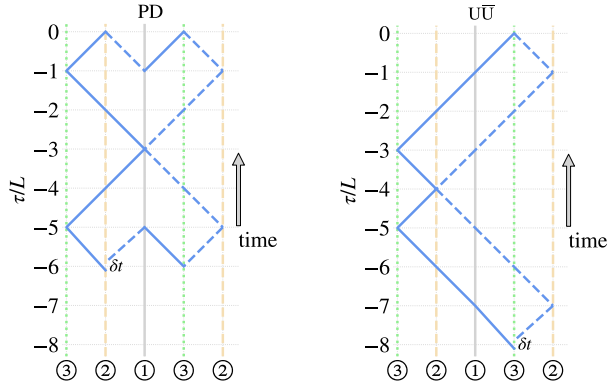

FIG. 3. The diagrams of the PD and $U\bar{U}$ channels.

$$\begin{aligned} \mathrm{PD}(t) &\approx \mathrm{P}(t+L) + \mathrm{D}(t-3L), \\ \mathrm{U}\bar{\mathrm{U}}(t) &\approx \mathrm{U}(t-4L) + \bar{\mathrm{U}}(t). \end{aligned} \tag{12}$$

Due to the symmetry of the Michelson and Sagnac configuration, the X_1 and α_1 also could essentially be obtained from this method. This approach could be extended to the various combinations from any two or more channels from the 15 first-generation channels, and we only select these two channels in this work.

(d) The last group is the Michelson-type TDI channels proposed in Dhurandhar *et al.* [23] which only employ two interferometer arms. A bunch of TDI channels could be derived from two arms/four links by using this approach. By defining a as the round trip along Arm3 (a: S/C1 → S/C2 → S/C1) and b as the round trip along Arm2 (b: S/C1 → S/C3 → S/C1), the X_{aabb} channel is selected to be investigated and expressed as

$$\begin{aligned} X_{aabb} &= [aabb, bbaa] \\ &\equiv aabbbbaa - bbaaaabb. \end{aligned} \tag{13}$$

The motivation for this selection is that this channel is the twice expanded X_1 channel and we may expect better performance than X_1 in a lower frequency band.

The investigations for these selected TDI channels will be implemented by following four steps:

(1) the TDI paths calculation using the algorithm in Sec. II A

(2) the GW response analysis for TDI channels in Sec. III
(3) the noise level evaluation of the channels in Sec. IV
(4) their sensitivities synthesis in Sec. V

III. GW RESPONSE

The response of a TDI channel to a GW signal is the combination of the response in every single link. The GW response formula for a single link has been specified in [54–57]. We reiterate the response formulation as follows:

For a GW source located at a direction (λ, β) in the solar-system barycentric (SSB) coordinates, where λ and β are the ecliptic longitude and latitude respectively, the propagation vector $\hat{k}$ is

$$\hat{\boldsymbol{k}} = -(\cos\lambda\cos\beta, \sin\lambda\cos\beta, \sin\beta). \tag{14}$$

The plus and cross polarization tensors of the GW signal are

$$\boldsymbol{e}_+ \equiv \mathcal{O}_1 \cdot \begin{pmatrix} 1 & 0 & 0 \\ 0 & -1 & 0 \\ 0 & 0 & 0 \end{pmatrix} \cdot \mathcal{O}_1^T,$$
$$\boldsymbol{e}_\times \equiv \mathcal{O}_1 \cdot \begin{pmatrix} 0 & 1 & 0 \\ 1 & 0 & 0 \\ 0 & 0 & 0 \end{pmatrix} \cdot \mathcal{O}_1^T, \tag{15}$$

with

$$\mathcal{O}_1 = \begin{pmatrix} \sin\lambda\cos\psi - \cos\lambda\sin\beta\sin\psi & -\sin\lambda\sin\psi - \cos\lambda\sin\beta\cos\psi & -\cos\lambda\cos\beta \\ -\cos\lambda\cos\psi - \sin\lambda\sin\beta\sin\psi & \cos\lambda\sin\psi - \sin\lambda\sin\beta\cos\psi & -\sin\lambda\cos\beta \\ \cos\beta\sin\psi & \cos\beta\cos\psi & -\sin\beta \end{pmatrix}, \tag{16}$$

where ψ is the polarization angle. The GW response in the lth link in TDI paths from the sender S/Cs to the receiver S/Cr is

$$y^h_{sr,l}(f, \Omega, \boldsymbol{r}_s, \boldsymbol{r}_r, l) = \frac{(1+\cos^2\iota)\hat{\boldsymbol{n}}_{sr}\cdot\boldsymbol{e}_+\cdot\hat{\boldsymbol{n}}_{sr} + i(-2\cos\iota)\hat{\boldsymbol{n}}_{sr}\cdot\boldsymbol{e}_\times\cdot\hat{\boldsymbol{n}}_{sr}}{4(1-\hat{\boldsymbol{n}}_{sr}\cdot\hat{\boldsymbol{k}})} \times [e^{2\pi i f(\hat{\boldsymbol{k}}\cdot\boldsymbol{r}_s - \tau_s)} - e^{2\pi i f(\hat{\boldsymbol{k}}\cdot\boldsymbol{r}_r - \tau_r)}], \tag{17}$$

where ι is the inclination angle of GW source, $\hat{\boldsymbol{n}}_{sr}$ is the unit vector from the sender S/Cs to the receiver S/Cr, and $\boldsymbol{r}_{s/r}$ is the position of the laser sender/receiver in the SSB coordinates as determined in the first step of the calculation. The $\hat{\boldsymbol{n}}_{sr}$ and $\boldsymbol{r}_{s/r}$ correspond to the values of lth link and the symbol l is omitted in the right part of Eq. (17).

As Eqs. (14)–(17) show, the response depends on four geometric angles $\Omega(\lambda, \beta, \psi, \iota)$, the GW frequency f, the time delay factors, and the positions of the sender and the receiver. Since the time delay and positions of the S/C have been determined in the first step as the results in Table I, the response of TDI for a given Ω will be straightforward to calculate along with all TDI links,

$$F^h_{\mathrm{TDI}}(f, \Omega) = \sum_{l=1}^{n} \mathrm{sgn}(\tau_l - \tau_{l-1}) y^h_{sr,l}(f, \Omega, \boldsymbol{r}_i, \boldsymbol{r}_j, l). \tag{18}$$

To evaluate the response for different Ω and frequency f in a yearly orbit, we randomly sample 10^5 sources in the $\Omega(\lambda, \beta, \psi, \iota)$ parameter space, and select the 26 time points in one year with a 14 day interval to calculate the responses in each TDI channel. This sampling method has been verified in Vallisneri and Galley [57] to achieve sufficient accuracy. The average response of one TDI channel to a monochromatic source in one year-observation will be

$$\mathcal{R}^2_{\mathrm{TDI}}(f, \Omega) = \frac{1}{T}\int_0^T |F^h_{\mathrm{TDI}}(f, \Omega)|^2 \mathrm{d}t, \tag{19}$$

where T is the observation time and is set to be one year. The median response to GW sources over the sky location, polarization, and inclination is employed to represent the responsiveness of each channel, and the curves are shown in Fig. 4. The differences of the GW response for TDI channels are the amplitudes at frequency region below 20 mHz and the spikes drop at their higher characteristic frequencies. The curve of the X_1 channel is treated as the fiducial response and is shown in both upper and lower panels. In the lower frequency band, the response of X_{aabb} is the highest in selected channels, and the response of T_2 is the lowest. The performance X_{aabb} is supposed to be the result that a double round trip along each arm can cumulate more low frequency GW signals and its links are the most in selected channels. For the response of the T_2 channel, based on our investigation for the T channel in Wang *et al.* [46], we infer that its low response is caused by cancellation from an equal part combination of X_1, X_2 and X_3, and the inequality between arms would increase its responsiveness. For other channels, the A_2 channel has a slightly higher response than X_1, and the response from the rest of the channels are modestly lower than X_1.

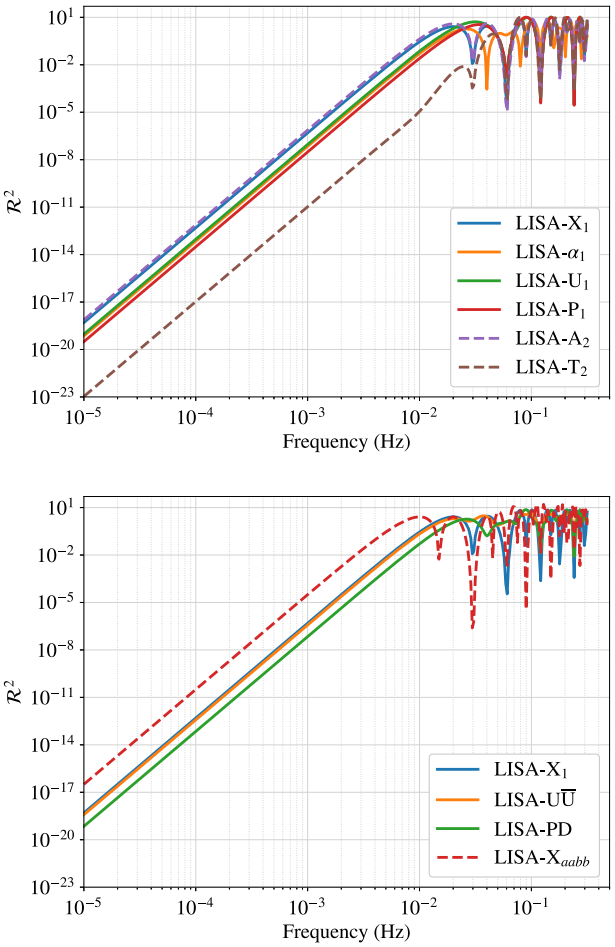

FIG. 4. The median responses of TDI channels in the frequency spectrum over one year and Ω (sky location λ and β, polarization ψ and inclination ι). The upper panel shows the first and second TDI groups, and the lower panel shows the third and fourth groups. The X_1 curve is treated as fiducial and shown also in the lower panel.

IV. NOISES IN TDI CHANNELS

TDI targets to suppress laser frequency noise beneath the secondary noises. The first-generation TDI configurations can not sufficiently suppress the laser frequency noise for LISA as we investigated in Wang *et al.* [44]. In this section, we investigate the residual laser noise and the secondary core noise (acceleration noise and optical path noise) levels in selected second-generation TDI channels. Other secondary noises (for instance, clock noise and tilt-to-length noise) are supposed to be resolved by the new designs and methods in [24,28–32]. By substituting Eqs. (A1) and (A2) into Eqs. (2) and (20) and summing up noises along the paths, we can obtain the noise level for a given TDI channel,

$$S_{n,TDI} = \left| \sum_{l=1}^{n} \mathrm{sgn}(\tau_l - \tau_{l-1}) \tilde{\eta}_{ij,l}(t_m + \tau_{j,l}) \right|^2, \quad (20)$$

where n is the number of links in a TDI channel, and $\tilde{\eta}$ is the amplitude spectral density of η. We decompose the laser frequency noise and secondary noise to show the impact of laser noise suppression and secondary noise level.

A. Laser frequency noise

The laser noise terms after TDI combination could be obtained by substituting Eqs. (A1)–(A2) and (2) into (5). For instance, the laser noise in the first-generation Michelson-X will be [44]

$$X_{laser}(t) = C_{12}(t_m + \tau_{1,0}) - C_{12}(t_m + \tau_{1,8}), \quad (21)$$

where C_{12} is the noise from laser source on the optical bench S/C1 pointing to S/C2 (as described in Appendix), $\tau_{1,0}$ and $\tau_{1,8}$ are the first and last values of τ in Table I, respectively. And the mismatch between two laser paths is $\delta t = \tau_{1,0} - \tau_{1,8}$. The amplitude of the Fourier components of residual laser noise would be [19]

$$\begin{aligned} |\tilde{X}_{laser}| &\simeq 2\pi f |\tau_{1,0} - \tau_{1,8}||\tilde{C}(f)| \\ &\simeq 2\pi f |\delta t||\tilde{C}(f)|, \end{aligned} \quad (22)$$

where $\tilde{C}(f) \simeq 1 \times 10^{-13}/\sqrt{\text{Hz}}$ is the one-sided square-root spectrum density of the Nd:YAG laser requirement for LISA [47].

By employing a set of 2200 days numerical orbit for LISA [42,46], the mismatching time for each TDI channel is calculated for each day using the algorithm in Sec. II A, and their cumulative histograms are shown in Fig. 5. By

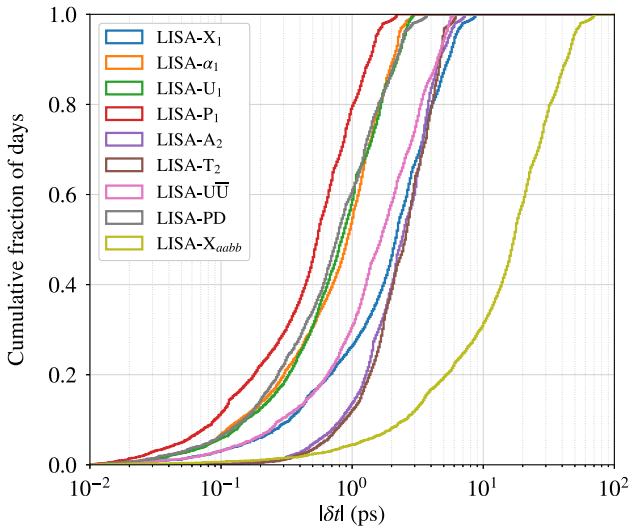

FIG. 5. The cumulative histograms of path mismatches for selected TDI channels. By employing a set of 2200 days numerical orbit for the LISA mission [42,46], the laser path mismatch of a TDI is calculated for each day (one point per day). The levels of path mismatch increases with longer time delay involved in TDI as reflected in Figs. 2 and 3 and Eq. (13).

assuming that the mismatch in 100 ns (30 m) is sufficient for laser noise cancellation for LISA [16], all the selected channels satisfy the requirement by several orders lower and can suppress laser noise effectively. The levels of path mismatch are varying with TDI channels, and we infer that the mismatch of a TDI channel increases with a larger time span. This inference could be reflected in the diagrams in Figs. 2 and 3 and Eq. (13); the X_{aabb} channel with the largest mismatch has a longest time span ($16L$), the mismatches of X_1 and $U\bar{U}$ with $8L$ time range is larger than the channels expanded $6L$ (α_1, U_1, and PD), and P_1 has the least mismatch for its $5L$ time span.

B. Secondary noise

After the laser frequency noise is substantially suppressed by the second-generation TDI, the secondary noises (especially acceleration noise and optical path noise) become the dominant noise sources. By assuming that there is no correlation between the different test masses and optical benches, the noise level is evaluated by substituting the corresponding terms in Eqs. (A1) and (A2) into Eqs. (2) and (20). Considering the upper limits of requirements for acceleration noise $S_{n,acc}$ and optical path noise $S_{n,op}$ for the LISA mission [47]

$$\sqrt{S_{n,acc}} = 3\times10^{-15}\frac{m/s^2}{\sqrt{Hz}} \times\sqrt{1+\left(\frac{0.4\ mHz}{f}\right)^2}\sqrt{1+\left(\frac{f}{8\ mHz}\right)^4},$$
$$\sqrt{S_{n,op}} = 10\times10^{-12}\frac{m}{\sqrt{Hz}}\sqrt{1+\left(\frac{2\ mHz}{f}\right)^4}. \quad (23)$$

The noise levels for selected TDI channels are shown in Fig. 6. The upper panel shows the noise power spectrum density (PSD) of TDI channels in the first group (X_1, α_1, U_1, and P_1) and optimal channels (A_2 and T_2), and the lower panel shows noise PSD in TDI channels $U\bar{U}$, PD, and X_{aabb}. By employing an unequal-arm numerical calculation, we find that the noise PSD of T_2 channel has a visible variance with time (or with the inequality of arm lengths) for frequencies lower than 1 mHz, and this phenomenon also appeared in the PSD calculation for the first-generation T channel as shown in Wang *et al.* [44]. For the T_2 channel, the dark gray in the upper panel shows the 50th percentile highest noise level in the first 300 days, and the light gray together with the dark gray shows the 90th percentile noise level in 300 days.

For the TDI channels in the first group, their PSD is approximately proportional to $4\sin^2(n\pi fL)$ of their corresponding first-generation TDI PSDs, where n is the number of time shifted arm lengths L between two first-generation TDI channels as shown in Eq. (10) and Fig. 2. Therefore, the first dropping spike appears at

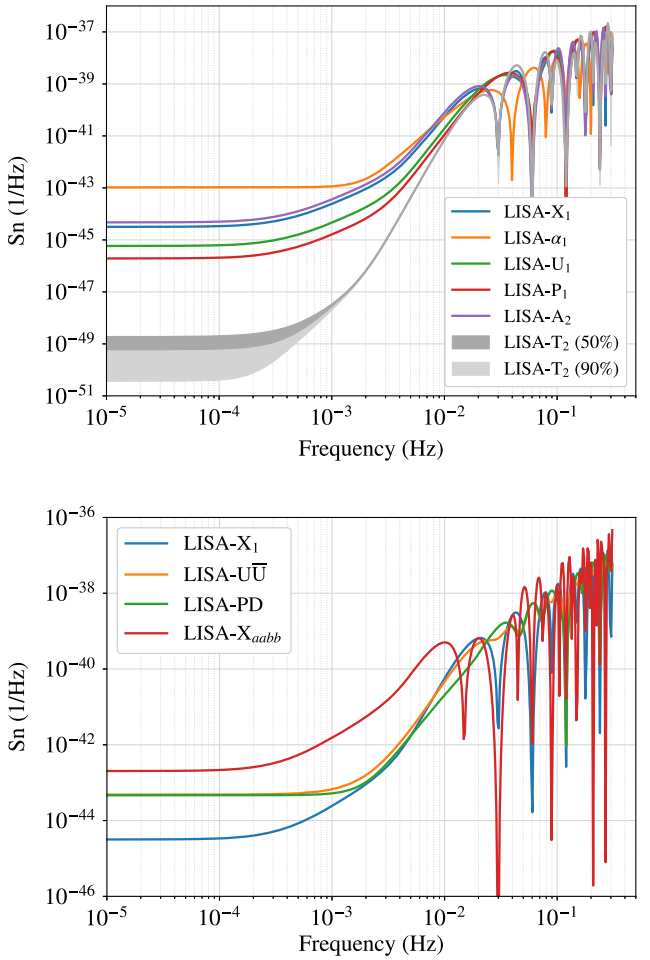

FIG. 6. The secondary noise PSD of selected TDI channels in the frequency spectrum. The upper panel shows the noise PSD in the first group channels (X_1, α_1, U_1, and P_1) and optimal channels (A_2 and T_2), and lower panel shows noise PSD in the channels $U\bar{U}$, PD and X_{aabb}. The dark gray in upper panel shows the 50th percentile highest noise level in the T_2 channel in the first 300 mission days, and the light gray together with the dark gray shows the 90th percentile noise level.

$f = 1/(4L) \simeq 0.03$ Hz for X_1, A_2 and T_2, $f = 1/(3L) \simeq 0.04$ Hz for α_1, $f = 1/(2L) \simeq 0.06$ Hz for U_1 and P_1, and $f = 1/(8L) \simeq 0.015$ Hz for X_{aabb} channel. The rule is not adaptable for the $U\bar{U}$ and PD channels which utilize two different first-generation channels.

V. SENSITIVITIES OF TDI CHANNELS

Based on the response and noise level for a GW source with Ω (ecliptic longitude λ, latitude β, polarization ψ, inclination ι), the optimal signal-to-noise ratio (SNR), ρ_{opt}, for one mission will be the joint SNRs from three optimal TDI channels (A_2, E_2, T_2) [19]

$$\rho^2_{opt} = \int_{f_{min}}^{f_{max}} \sum_{A_2,E_2,T_2} \frac{|F^h_{TDI}(f,L,\Omega) * \tilde{h}(f)|^2}{S_{n,TDI}(f,L)} df, \quad (24)$$

where $\tilde{h}(f)$ is the GW signal in the frequency domain. The instantaneous optimal sensitivity, $S_{opt}(f, L, \Omega)$, could be derived from Eq. (24) as [19]

$$S_{opt}(f, L, \Omega) = \left[\sum_{A_2,E_2,T_2} \frac{|F^h_{TDI}(f, L, \Omega)|^2}{S_{n,TDI}(f, L)}\right]^{-1}, \quad (25)$$

where S_{opt} represents the strain precision which could be measured when the six laser links of mission are functional. The constellation orbital motions and time-varying arm lengths, $F^h_{TDI}(f, L, \Omega)$ and $S_{n,TDI}(f, L)$ will change with mission time, especially for the T_2 channel. Therefore, the yearly averaged sensitivity for a source with Ω could evaluated as

$$\begin{aligned}\bar{S}_{opt}(f, \Omega) &= \left[\sum_{A_2,E_2,T_2} \left\langle \frac{|F^h_{TDI}(f, L, \Omega)|^2}{S_{n,TDI}(f, L)} \right\rangle_{1\ yr}\right]^{-1} \\ &= \left[\sum_{A_2,E_2,T_2} \frac{1}{T}\int_0^T \frac{|F^h_{TDI}(f, L, \Omega)|^2}{S_{n,TDI}(f, L)} dt\right]^{-1}. \quad (26)\end{aligned}$$

The yearly averaged sensitivity for a single TDI channel will be

$$\bar{S}_{TDI}(f, \Omega) = \left[\frac{1}{T}\int_0^T \frac{|F^h_{TDI}(f, L, \Omega)|^2}{S_{n,TDI}(f, L)} dt\right]^{-1}. \quad (27)$$

To make following content more readable, we clarify that $S_{n,TDI}$ denotes the noise PSD from the instruments and measurements in a TDI channel, and S_{TDI} is the sensitivity of a TDI channel which is the GW response weighted $S_{n,TDI}$.

As we can expect, the sensitivity of a TDI channel will be different for various $\Omega(\lambda, \beta, \psi, \iota)$; the histograms of sensitivities at 10 mHz for multiple channels are shown in inset plots of the lower panels of Fig. 7. Compared to the single channel becoming worse with a longer sensitivity tail, the histogram of joint $A_2 + E_2 + T_2$ channel narrows down the sensitivity range which indicates the more homogeneous space coverage. The most sensitive direction is around the ecliptic plane, while the insensitive direction is around the ecliptic polar directions in a one-year observation as shown in Fig. 8. The mean value of sensitivity over Ω is ~1.1 times worse than its median value. The curve of median values is employed to represent the performance of each TDI channel over Ω parameter space, and the curves of selected channels are shown in Fig. 7. Note that, this sensitivity is

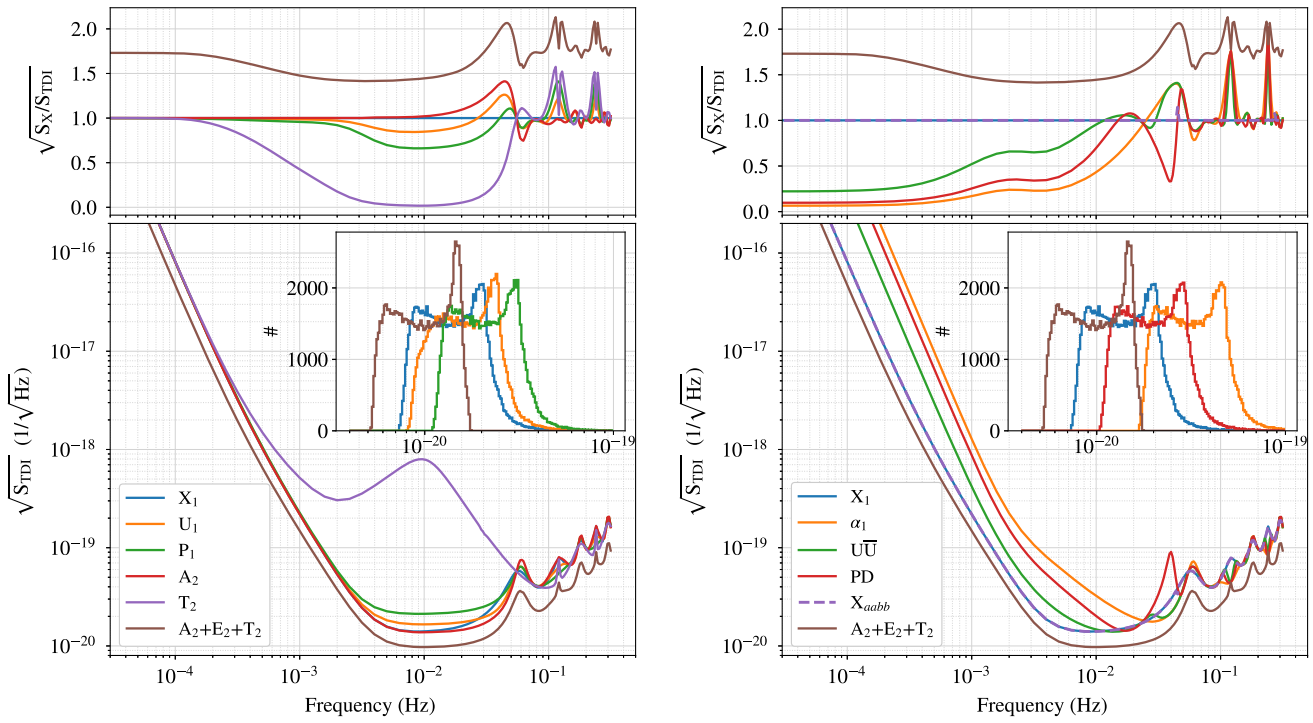

FIG. 7. The yearly median sensitivity over $\Omega(\lambda, \beta, \psi, \iota)$ for selected TDI channels. The left panel shows the curves for channels X_1, U_1, and P_1 and optimal channels (A_2 and T_2), and the right panel shows channels α_1, $U\bar{U}$, PD and X_{aabb} as well as X_1. The joint sensitivity $A_2 + E_2 + T_2$ is plotted in both panels for comparison. The upper panels show the sensitivity ratios between fiducial first-generation laser noise free Michelson-X and selected channels, $\sqrt{S_X/S_{TDI}}$. The inset plots in the lower panels show the histograms of sensitivities at 10 mHz for multiple channels. Note that, these sensitivities are averaged over the sky location, polarization and inclination $\Omega(\lambda, \beta, \psi, \iota)$; the sensitivity over sky location and polarization $(\lambda, \beta, \psi, \iota = 0)$ will be lower than these results by a factor of $\frac{8}{5\pi} \simeq 0.51$.

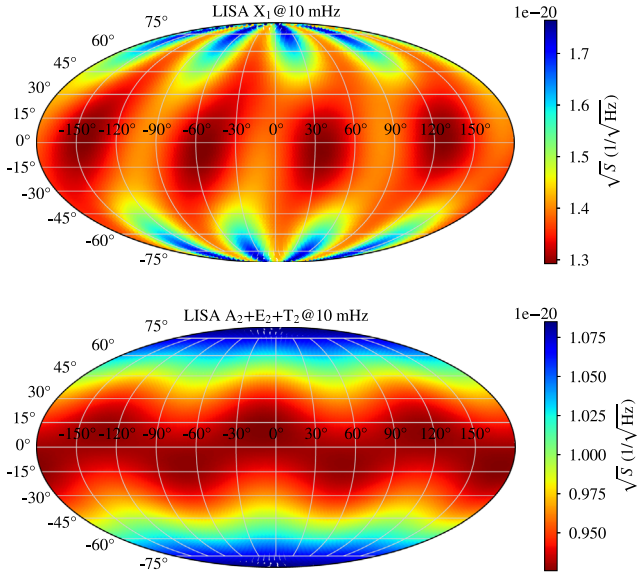

FIG. 8. The yearly averaged sensitivity distribution on sky map for the X_1 (upper panel) and the joint optimal A_2, E_2 and T_2 (lower panel) channels at 10 mHz in the solar system barycentric ecliptic coordinates. The sensitivity is calculated by fixing the polarization ($\psi = \pi/6$) and inclination ($\iota = \pi/3$).

averaged over sky location, polarization and inclination (λ, β, ψ, ι); the sky location and polarization (λ, β, ψ, $\iota = 0$) averaged sensitivity will be lower than these results by a factor of $\frac{8}{5\pi} \simeq 0.51$.

The curves of yearly averaged median sensitivity over Ω for channels (X_1, α_1, U_1, P_1, A_2, and T_2) are shown in the left panel of Fig. 7, and curves for other channels (X_1, α_1, $U\bar{U}$, PD, and X_{aabb}) are shown in the right panel, as well as the curves of X_1 and $A_2 + E_2 + T_2$ in both panels for comparison. As we can see from the left plot, compared to the first-generation TDI channels shown in [44,46], the sensitivities of channels (X_1, U_1 and P_1, A_2 and T_2) are expected to be equal to their corresponding first-generation TDI channels when the laser frequency noise is not considered. The sensitivity of the T_2 channel is irregular and should be the result of unequal arm configuration as we investigated in [44,46]. The joint $A_2 + E_2 + T_2$ channel not only improves the sensitivity of X_1 by a factor of $\sqrt{2}$ to $\sqrt{3}$ for frequencies lower than 30 mHz, and by a factor of two at some higher frequencies as shown in the upper panel, it also achieves a better sky coverage as shown by the histograms in the inset plots.

The major differences of sensitivities in the right panel of Fig. 7 are in frequency range lower than 20 mHz. The sensitivity of α_1 channel is the worst in selected channels at lower frequencies. However, it can reach a relatively good level at some higher frequencies (e.g., 30 mHz, 120 mHz). The PD channel has the second worse sensitivity at low frequencies, and reach ~2 times better than X_1 at frequencies 0.12 Hz and 0.24 Hz. The $U\bar{U}$ channel has a worse sensitivity than the X_1 channel in the lower frequency band, and has better sensitivity at some frequencies. The sensitivity of X_{aabb} is identical to X_1 even though its response in the lower frequency band is higher than X_1, the higher noise level counteracts the advantage in response. We infer that all Michelson-like TDI combinations have identical sensitivity since the GW response and the noise level are proportional.

On the other hand, to illustrate the sensitivity variation with the sky locations of GW sources, with the fixed polarization and inclination ($\psi = \pi/6$, $\iota = \pi/3$), the yearly averaged sensitivity of X_1 and joint $A_2 + E_2 + T_2$ channels at 10 mHz are shown in Fig. 8. As expected, with the orbital motion of 60° tilted array, the sources located around the ecliptic plane could be observed with better antenna pattern modulation and hence better sensitivity, and polar directions are observed with the worst sensitivities. Another factor is that the sources at the same latitude could not be observed with equal sensitivity as shown in the upper panel for the X_1 channel, and this should be due to the geometric angles between polarization and selected interferometric arms and their yearly orbital motion. Without considering the variations of polarization and inclination, the sensitivity range for the insensitive polar directions and sensitive ecliptic plane directions becomes more concentrated compared to the results considering the Ω four parameters.

VI. CONCLUSIONS

In this work, we introduce a generic algorithm to investigate the performance of TDI. By employing a numerical mission orbit for LISA, as the first step, the algorithm determines the time delays and S/C positions in a realistic dynamical case. Then the algorithm can numerically evaluate the GW response, PSD of noise sources, and sensitivity for a TDI channel based on the obtained time delays and S/C positions. As assistance to sequence the links in TDI, a S/C layout-time delay diagram is developed to streamline the calculation procedures in the algorithm. The algorithm should be feasible for any TDI observable and other missions employing the TDI technology.

We select 11 second-generation TDI channels constructed from four approaches and implement our algorithm for their performance investigations. Based on the numerical results, the interference paths of selected TDI channels are well matched and the laser frequency noise should be sufficiently suppressed beneath the secondary noise. Without considering laser frequency noise and only including secondary core noises (acceleration noise and optical path noise), the second-generation TDI channels composed from the two same first-generation channels would have equivalent sensitivities as their corresponding first-generation channels. This is also applicable to the optimal TDI channels (A_2, E_2, and T_2) combined from the second-generation Michelson channels (X_1, X_2, and X_3) compared

to the first-generation optimal channels (A, E and T). The joint $A_2 + E_2 + T_2$ channel would have $\sqrt{2}$ to 2 times better sensitivity than X_1 channel in the full frequency band, and the joint observation could also cover all sky directions with more even sensitivity. In a one-year observation, the sensitive direction is around the ecliptic plane, while the insensitive directions are around the ecliptic polar.

The Sagnac α_1 together with PD and UŪ channels have the worst sensitivity in the low-frequency band compared to the fiducial X_1 channel, although they could have better sensitivities at multiple characteristic higher frequencies. For the Michelson-like channels which employ four links from two arms, X, X_1, and X_{aabb} are investigated, and their sensitivities are identical when the secondary core noises are considered. Even X_{aabb} channel improves the GW response in the low-frequency band, the increase of noise level from longer path counteracts the gain of the GW response. And all Michelson-like TDI channels are inferred to have equal sensitivity.

ACKNOWLEDGMENTS

This work was supported by NSFC Grants No. 12003059 and No. 11773059, Key Research Program of Frontier Sciences, Chinese Academy of Science, Grant No. QYZDB-SSW-SYS016, and the Strategic Priority Research Program of the Chinese Academy of Sciences under Grants No. XDA1502070102, No. XDA15020700, No. XDB21010100, No. XDB23030100, and No. XDB23040000. This work was also supported by the National Key Research and Development Program of China under Grants No. 2016YFA0302002 and No. 2017YFC0601602. This work made use of the High Performance Computing Resource in the Core Facility for Advanced Research Computing at Shanghai Astronomical Observatory.

APPENDIX: THE OBSERVABLES ON OPTICAL BENCHES

Observables s_{ji}, ε_{ij} and τ_{ij} (for $j = \mathrm{S/C2} \to i = \mathrm{S/C1}$, $\mathrm{S/C3} \to \mathrm{S/C2}$ and $\mathrm{S/C1} \to \mathrm{S/C3}$)

$$\begin{aligned} s_{ji} &= y_{ji}^{h} : h + \mathcal{D}_{ji} C_{ji}(t) - C_{ij}(t) \\ &\quad + \mathcal{D}_{ji} N_{ji}^{\mathrm{OB}}(t) - N_{ij}^{\mathrm{OB}}(t) + n_{ij}^{\mathrm{op}}(t), \\ \varepsilon_{ij} &= C_{ik}(t) - C_{ij}(t) + 2n_{ij}^{\mathrm{acc}}(t) - 2N_{ij}^{\mathrm{OB}}(t), \\ \tau_{ij} &= C_{ik}(t) - C_{ij}(t), \end{aligned} \tag{A1}$$

and observables s_{ij}, ε_{ij} and τ_{ij} (for $1 \to 2, 2 \to 3$ and $3 \to 1$)

$$\begin{aligned} s_{ji} &= y_{ji}^{h} : h + \mathcal{D}_{ji} C_{ji}(t) - C_{ij}(t) \\ &\quad - \mathcal{D}_{ji} N_{ji}^{\mathrm{OB}}(t) + N_{ij}^{\mathrm{OB}}(t) + n_{ij}^{\mathrm{op}}(t), \\ \varepsilon_{ij} &= C_{ik}(t) - C_{ij}(t) - 2n_{ij}^{\mathrm{acc}}(t) + 2N_{ij}^{\mathrm{OB}}(t), \\ \tau_{ij} &= C_{ik}(t) - C_{ij}(t). \end{aligned} \tag{A2}$$

The symbols are specified as follows:

(a) y_{ji}^{h} is the response function to the GW signal h.
(b) C_{ij} denotes laser noise on the optical bench in S/Ci pointing to S/Cj.
(c) N_{ij}^{OB} is the effect from displacement along the arm L_{ji} for the optical bench on S/Ci pointing to S/Cj.
(d) L_{ij} is the arm length or propagation time from S/Ci to j which includes the relativistic delay caused by gravitational field. The L_{ij} and L_{ji} are treated as unequal in this dynamical scenario, and the calculation is described by Eq. (7).
(e) n_{ij}^{op} represents the optical path noise on the S/Ci pointing to j.
(f) n_{ij}^{acc} denotes the acceleration noise from test mass on the S/Ci pointing to j.

[1] B. P. Abbott *et al.* (LIGO Scientific Collaboration and Virgo Collaboration), Observation of Gravitational Waves from a Binary Black Hole Merger, Phys. Rev. Lett. **116**, 061102 (2016), and references therein.
[2] B. P. Abbott *et al.* (LIGO Scientific Collaboration and Virgo Collaboration), Binary Black Hole Mergers in the first Advanced LIGO Observing Run, Phys. Rev. X **6**, 041015 (2016); Erratum, Phys. Rev. X **8**, 039903 (2018).
[3] B. P. Abbott *et al.* (LIGO Scientific Collaboration and Virgo Collaboration), GW170817: Observation of Gravitational Waves from a Binary Neutron Star Inspiral, Phys. Rev. Lett. **119**, 161101 (2017).
[4] B. P. Abbott *et al.* (LIGO Scientific Collaboration and Virgo Collaboration), GWTC-1: A Gravitational-Wave Transient Catalog of Compact Binary Mergers Observed by LIGO and Virgo during the First and Second Observing Runs, Phys. Rev. X **9**, 031040 (2019).
[5] A. H. Nitz, T. Dent, G. S. Davies, S. Kumar, C. D. Capano, I. Harry, S. Mozzon, L. Nuttall, A. Lundgren, and M. Tápai, 2-OGC: Open gravitational-wave catalog of binary mergers from analysis of public Advanced LIGO and Virgo data, Astrophys. J. **891**, 123 (2020).
[6] B. Abbott *et al.* (LIGO Scientific, Virgo Collaborations), GW190425: Observation of a compact binary coalescence with total mass $\sim 3.4\ M_{\odot}$, Astrophys. J. Lett. **892**, L3 (2020).
[7] R. Abbott *et al.* (LIGO Scientific, Virgo Collaborations), GW190412: Observation of a binary-black-hole coalescence

with asymmetric masses, Phys. Rev. D **102**, 043015 (2020).
[8] R. Abbott *et al.* (LIGO Scientific, Virgo Collaborations), GW190814: Gravitational waves from the coalescence of a 23 solar mass black hole with a 2.6 solar mass compact object, Astrophys. J. **896**, L44 (2020).
[9] R. Abbott *et al.*, GWTC-2: Compact binary coalescences observed by LIGO and Virgo during the first half of the third observing run, arXiv:2010.14527 [Phys. Rev. X (to be published)].
[10] R. Abbott *et al.* (LIGO Scientific, Virgo Collaborations), GW190521: A Binary Black Hole Merger with a Total Mass of 150 $M_\odot$, Phys. Rev. Lett. **125**, 101102 (2020).
[11] J. W. Armstrong, F. B. Estabrook, and M. Tinto, Time-delay interferometry for space-based gravitational wave searches, Astrophys. J. **527**, 814 (1999).
[12] F. B. Estabrook, M. Tinto, and J. W. Armstrong, Time-delay analysis of LISA gravitational wave data: Elimination of spacecraft motion effects, Phys. Rev. D **62**, 042002 (2000).
[13] J. W. Armstrong, F. B. Estabrook, and M. Tinto, Sensitivities of alternate LISA configurations, Classical Quant. Grav. **18**, 4059 (2001).
[14] S. L. Larson, R. W. Hellings, and W. A. Hiscock, Unequal arm space borne gravitational wave detectors, Phys. Rev. D **66**, 062001 (2002).
[15] S. V. Dhurandhar, K. Rajesh Nayak, and J. Y. Vinet, Algebraic approach to time-delay data analysis for LISA, Phys. Rev. D **65**, 102002 (2002).
[16] M. Tinto, D. A. Shaddock, J. Sylvestre, and J. W. Armstrong, Implementation of time-delay interferometry for LISA, Phys. Rev. D **67**, 122003 (2003).
[17] M. Vallisneri, Synthetic LISA: Simulating time delay interferometry in a model LISA, Phys. Rev. D **71**, 022001 (2005).
[18] A. Petiteau, G. Auger, H. Halloin, O. Jeannin, E. Plagnol, S. Pireaux, T. Regimbau, and J.-Y. Vinet, LISACode: A scientific simulator of LISA, Phys. Rev. D **77**, 023002 (2008).
[19] M. Tinto and S. V. Dhurandhar, Time-delay interferometry, Living Rev. Relativity **24**, 1 (2021).
[20] D. A. Shaddock, M. Tinto, F. B. Estabrook, and J. Armstrong, Data combinations accounting for LISA spacecraft motion, Phys. Rev. D **68**, 061303 (2003).
[21] N. J. Cornish and R. W. Hellings, The effects of orbital motion on LISA time delay interferometry, Classical Quant. Grav. **20**, 4851 (2003).
[22] M. Tinto, F. B. Estabrook, and J. Armstrong, Time delay interferometry with moving spacecraft arrays, Phys. Rev. D **69**, 082001 (2004).
[23] S. Dhurandhar, K. Nayak, and J. Vinet, Time delay interferometry for LISA with one arm dysfunctional, Classical Quant. Grav. **27**, 135013 (2010).
[24] M. Tinto and O. Hartwig, Time-delay interferometry and clock-noise calibration, Phys. Rev. D **98**, 042003 (2018).
[25] J.-B. Bayle, M. Lilley, A. Petiteau, and H. Halloin, Effect of filters on the time-delay interferometry residual laser noise for LISA, Phys. Rev. D **99**, 084023 (2019).
[26] M. Muratore, D. Vetrugno, and S. Vitale, Revisitation of time delay interferometry combinations that suppress laser noise in LISA, Classical Quant. Grav. **37**, 185019 (2020).
[27] M. Vallisneri, J.-B. Bayle, S. Babak, and A. Petiteau, TDI-infinity: Time-delay interferometry without delays, Phys. Rev. D **103**, 082001 (2021).
[28] M. Otto, G. Heinzel, and K. Danzmann, TDI and clock noise removal for the split interferometry configuration of LISA, Classical Quant. Grav. **29**, 205003 (2012).
[29] M. Otto, Time-Delay Interferometry Simulations for the Laser Interferometer Space Antenna, Ph.D. thesis Gottfried Wilhelm Leibniz Universität Hannover, Diss., (2015), https://www.repo.uni-hannover.de/handle/123456789/8598?locale-attribute=en.
[30] O. Hartwig and J.-B. Bayle, Clock-jitter reduction in LISA time-delay interferometry combinations, arXiv:2005.02430.
[31] M. Chwalla *et al.*, Design and construction of an optical test bed for LISA imaging systems and tilt-to-length coupling, Classical Quant. Grav. **33**, 245015 (2016).
[32] M. Tröbs *et al.*, Reducing tilt-to-length coupling for the LISA test mass interferometer, Classical Quant. Grav. **35**, 105001 (2018).
[33] N. J. Cornish and L. J. Rubbo, LISA response function, Phys. Rev. D **67**, 022001 (2003).
[34] L. J. Rubbo, N. J. Cornish, and O. Poujade, Forward modeling of space-borne gravitational wave detectors, Phys. Rev. D **69**, 082003 (2004).
[35] W.-T. Ni, ASTROD-GW: Overview and progress, Int. J. Mod. Phys. D **22**, 1341004 (2013).
[36] G. Wang, Time-delay Interferometry for ASTROD-GW, Master thesis, Purple Mountain Observatory, Chinese Academy of Sciences, Nanjing, (2011).
[37] G. Wang and W.-T. Ni, Time-delay interferometry for ASTROD-GW, Chin. Astron. Astrophys. **36**, 211 (2012), and references therein.
[38] G. Wang and W.-T. Ni, Numermcal simulation of time delay interferometry for NGO/eLISA, Classical Quant. Grav. **30**, 065011 (2013).
[39] G. Wang and W.-T. Ni, Orbit optimization for ASTROD-GW and its time delay interferometry with two arms using CGC ephemeris, Chin. Phys. B **22**, 049501 (2013).
[40] S. V. Dhurandhar, W. T. Ni, and G. Wang, Numerical simulation of time delay interferometry for a LISA-like mission with the simplification of having only one interferometer, Adv. Space Res. **51**, 198 (2013).
[41] G. Wang and W.-T. Ni, Orbit optimization and time delay interferometry for inclined ASTROD-GW formation with half-year precession-period, Chin. Phys. B **24**, 059501 (2015).
[42] G. Wang and W.-T. Ni, Numerical simulation of time delay interferometry for TAIJI and new LISA, Res. Astron. Astrophys. **19**, 058 (2019).
[43] G. Wang, W.-T. Ni, and A.-M. Wu, Orbit design and thruster requirement for various constant-arm space mission concepts for gravitational-wave observation, Int. J. Mod. Phys. D **29**, 1940006 (2020).
[44] G. Wang, W.-T. Ni, and W.-B. Han, Revisiting time delay interferometry for unequal-arm LISA and TAIJI, (Paper I), arXiv:2008.05812.
[45] M. Vallisneri, Geometric time delay interferometry, Phys. Rev. D **72**, 042003 (2005); Erratum, Phys. Rev. D **76**, 109903 (2007).

[46] G. Wang, W.-T. Ni, W.-B. Han, S.-C. Yang, and X.-Y. Zhong, Numerical simulation of sky localization for LISA-TAIJI joint observation, Phys. Rev. D **102**, 024089 (2020).
[47] P. Amaro-Seoane, H. Audley, S. Babak, and *et al.* (LISA Team), Laser interferometer space antenna, arXiv:1702.00786.
[48] N. Ashby and P. L. Bender, Measurement of the shapiro time delay between drag-free spacecraft, Astrophysics and Space Science Library **349**, 219 (2008).
[49] I. I. Shapiro, Fourth Test of General Relativity, Phys. Rev. Lett. **13**, 789 (1964).
[50] S. M. Kopeikin, Post-Newtonian limitations on measurement of the PPN parameters caused by motion of gravitating bodies, Mon. Not. R. Astron. Soc. **399**, 1539 (2009).
[51] X. X. Newhall, Numerical representation of planetary ephemerides, Celest. Mech. **45**, 305 (1988).
[52] G. Li and L. Tian, PMOE 2003 Planetary ephemeris framework (V) creating and using of ephemeris files, Publ. Purple Mountain Astron. Obs. **23**, 160 (2004).
[53] T. A. Prince, M. Tinto, S. L. Larson, and J. W. Armstrong, The LISA optimal sensitivity, Phys. Rev. D **66**, 122002 (2002).
[54] M. Vallisneri, J. Crowder, and M. Tinto, Sensitivity and parameter-estimation precision for alternate LISA configurations, Classical Quant. Grav. **25**, 065005 (2008).
[55] F. B. Estabrook and H. D. Wahlquist, Response of Doppler spacecraft tracking to gravitational radiation., Gen. Relativ. Gravit. **6**, 439 (1975).
[56] H. Wahlquist, The Doppler response to gravitational waves from a binary star source, Gen. Relativ. Gravit. **19**, 1101 (1987).
[57] M. Vallisneri and C. R. Galley, Non-sky-averaged sensitivity curves for space-based gravitational-wave observatories, Classical Quant. Grav. **29**, 124015 (2012).